Dalton Transactions

The Zintl phases AIn2As2 (A = Ca, Sr, Ba): New topological insulators and thermoelectric material candidates

Journal:	*Dalton Transactions*
Manuscript ID	DT-ART-05-2021-001521.R1
Article Type:	Paper
Date Submitted by the Author:	04-Jun-2021
Complete List of Authors:	Ogunbunmi, Michael; University of Delaware, Chemistry and Biochemistry Baranets, Sviatoslav; University of Delaware, Chemistry and Biochemistry Childs, Amanda; University of Delaware, Department of Chemistry and Biochemistry Bobev, Svilen; University of Delaware, Chemistry and Biochemistry

Dalton Transactions

ARTICLE

The Zintl phases AIn_2As_2 (A = Ca, Sr, Ba): New topological insulators and thermoelectric material candidates

Received 00th January 20xx,
Accepted 00th January 20xx

DOI: 10.1039/x0xx00000x

www.rsc.org/

Michael O. Ogunbunmi[a], Sviatoslav Baranets[a], Amanda B. Childs[a] and Svilen Bobev*[a]

Recently, there has been a lot of interest in topological insulators (TIs), being electronic materials, which are insulating in their bulk but with the gapless exotic metallic state on their surface. The surface states observed in such materials behave as a perfect conductor thereby making them more suited for several cutting-edge technological applications such as spintronic devices. Here, we report the synthesis and structural characterization of the Zintl phases AIn_2As_2 (A = Ca, Sr, Ba), which could become a new class of TIs. Crystal structure elucidation by single-crystal X-ray diffraction reveals that $CaIn_2As_2$ and $SrIn_2As_2$ are isostructural and crystallize in the $EuIn_2P_2$ structure type (space group $P6_3/mmc$, No. 194, Z = 2) with unit cell parameters a = 4.1482(6) Å, c = 17.726(4) Å; and a = 4.2222(6) Å, c = 18.110(3) Å, respectively. Their hexagonal structure is made up of alternating $[In_2As_2]^{2-}$ layers separated by slabs of A^{2+} cations. $BaIn_2As_2$ on the other hand crystallizes in the monoclinic $EuGa_2P_2$ structure type (space group $P2/m$, No. 10, Z = 4) with unit cell parameters a = 10.2746(11) Å, b = 4.3005(5) Å, c = 13.3317(14) Å and β = 95.569(2)°. This structure is also layered, and it is made up of different type of polyanionic $[In_2As_2]^{2-}$ units and Ba^{2+} cations. The valence electron count for all three compounds adheres to the Zintl-Klemm formalism, and all elements achieve closed-shell electronic configurations. Bulk electronic structure calculations indicate the opening of a bandgap E_g ~ 0.03 eV ($CaIn_2As_2$ and $Sr_2In_2As_2$), and E_g ~0.21 eV ($BaIn_2As_2$) in the absence of strain and spin-orbit coupling (SOC). These results argue in favor of the realization of a nontrivial topological insulator state under the influence of tensile strain and SOC. Preliminary transport properties on $BaIn_2As_2$ are suggestive of a degenerate p-type semiconductor—a behavior which is sought after in thermoelectric (TE) materials. Since both TIs and excellent TE materials are known to favor the same material properties such as narrow bandgap, heavy elements, and strong SOC, these three Zintl phases are also projected as candidates TE materials.

Introduction

The classification of quantum materials exhibiting novel phases of matter is of great interest to physicists and chemists alike as such classification helps to explore their properties and prospective applications. To classify materials, the knowledge of the order parameter is important, and this is characterized based on the underlying symmetries that are spontaneously broken[1]. However, the quantum hall effect, discovered over 3 decades ago presents an example of a state that does not break any symmetries but depends on the topology of the material. Consequently, a new classification that is based on topological order was birthed and provides us with an in-depth understanding of various exotic forms of matter[2,3]. With increasing research activities, several new phases such as the quantum spin Hall states (Topological insulators)[4] have been observed. Topological insulators (TIs) are electronic materials that are insulating in their bulk (having an energy gap between the valence band maximum and the conduction bands minimum) but with a gapless exotic metallic state on their surface. Their surface states are insensitive to scatterings by impurities and are topologically protected *i.e.*, the properties do not change with small deformation, due to effects of strong spin-orbit coupling (SOC) and time-reversal symmetry. In such a state, electrons of opposite spins (spin up and spin down) move in opposite directions in pairs with a spin-momentum locking, thereby exhibiting helicity. TIs are often identified by their characteristic fingerprints[5] which includes strong SOC, a sign reversal of the molecular orbital symmetry, and an odd number of band inversion between the conduction and the valence bands, all of which can be unmasked by angle-resolved photoemission spectroscopy (ARPES) and electronic structure calculations.

Due to the possibility of a dissipationless flow of electric current at the surface of TIs, they are being projected as key new materials for applications in spintronic devices, magneto-electronics, and quantum computers[6,7]. In addition, several TIs are known to possess excellent thermoelectric (TE) properties (which provide for the conversion of waste heat into electricity), as fingerprints found in TIs also favor excellent TE

[a] Department of Chemistry and Biochemistry, University of Delaware, Newark, Delaware 19716, United States

† Electronic Supplementary Information (ESI) available: Figures depicting the cation coordination, the In_2As_6 moieties, a side-by-side comparison between $BaIn_2P_2$ and $BaIn_2As_2$, electronic structure calculations for $SrIn_2As_2$. Results from the EDX analysis for a single crystal of $BaIn_2As_2$. CIFs from all refined structures have been deposited with the Cambridge Structural Database (CSD) of X-ray structural data and have access codes CCDC 2082408, 2082409, and 2082410. See DOI: 10.1039/x0xx00000x

properties[8]. This perceptivity on the Siamese nature of TI and excellent TE properties is therefore currently driving several research endeavours as it provides leverage to a more focused search and investigation of TE materials. This will no doubt bring about an improvement to the TE figure of merit zT ($zT = \alpha^2T/\rho\kappa$, α = Seebeck coefficient, T = temperature, ρ = electrical resistivity, κ = thermal conductivity)[9,10]. It has been shown that strong correlations and relationship exist between the surface states properties of a TI and the Seebeck coefficient of a TE material (as well as to other transport properties) such that tuning the surface state properties of a TI can lead to the enhancement of zT[11,12].

Zintl phases[13] which are compounds at the border of the typical valence-precise compounds and the intermetallics, tend to have closed-shell electronic configurations for the constituent elements. As a result, narrow bandgaps are abundant for such compounds, and many of them are known for their excellent TE properties or are being explored as candidate-materials for thermoelectrics.

The herein reported Zintl phase $BaIn_2As_2$ has the $EuGa_2P_2$ structure type (space group $P2/m$),[14] while the Ca- and Sr-compounds with the same composition crystallize with the layered hexagonal $EuIn_2P_2$ structure type (space group $P6_3/mmc$). Several compounds belonging to these classes have recently received attention due to their interesting topological properties—for example, in $EuIn_2As_2$,[15] a realization of colossal magnetoresistance (CMR) of magnitude −143% (T = 17.5 K, H = 5 T) has been reported. This compound also undergoes an antiferromagnetic ordering at T_N = 17 K. Similar observations are also made in $EuIn_2P_2$[16] with T_N = 24 K and CMR of −298% (T = 24, H = 5 T). The enhanced magnetoresistance in the phosphide compound is thought to be associated with its higher degree of magnetic coupling, compared to that of the arsenide[17]. $EuIn_2As_2$ is a magnetic insulator with an estimated bandgap, E_g = 0.1 eV along the Γ-M direction, and where the Eu^{2+} electronic state of $4f^7$ is localized. Depending on the orientation of the magnetic moments, the A-type AFM order in $EuIn_2As_2$ can lead to either an axion insulator (magnetic TI in which the nontrivial $\mathbb{Z}_2$ index is protected by inversion symmetry instead of time-reversal symmetry) or a higher-order topological insulator with chiral states existing on the hinges between the gapped surfaces. Hence, $EuIn_2As_2$ is proposed as a unique material, which provides a fertile playground to study the interplay of magnetic order and nontrivial topology. Other isostructural compounds reported to date include $CaIn_2P_2$ and $SrIn_2P_2$ phases[18]. Both compounds are narrow gap semiconductors with $CaIn_2P_2$ and $SrIn_2As_2$ having an indirect E_g = 0.39 eV and a direct E_g = 0.28 eV, respectively[19]. Furthermore, a quantum phase transition from a semiconductor to a nontrivial topological phase is reported in both compounds, where the application of a minimal strain leads to a band inversion and the subsequent opening of a bandgap along the line node in the presence of SOC[20,21]. Although not isotypic to AIn_2As_2 (A = Ca, Sr, Ba), here it is worth mentioning some other "1-2-2" Zintl pnictides that have gained prominence in recent years. Examples of such can be $EuSn_2As_2$[22,23], $EuMg_2Bi_2$[24-26], and $EuCd_2As_2$[27-31] (all three with the $CaAl_2Si_2$ structure type), where evidence of Dirac surface states and topological behaviors have been reported.

From the above introductory remarks, one can surmise that the rich exotic states within the realm of "1-2-2" Zintl phases are apparently underexplored. The three phases discussed in this paper will expand the toolbox for many scientists working in this field, and are expected to bolster the understanding of the exotic topological properties of matter.

Results and discussion

Synthesis

As detailed in the experimental section, single crystals of the title compounds can be readily grown from either In or Pb flux. The synthesis accommodates a flexible temperature profile with maximum reaction temperature between 1233 K and 1373 K. The use of indium self-flux is arguably the more robust approach, yet, it should be noted that the grown crystals were small and are barely suitable for physical properties measurements. Also, we found flux reactions in alumina crucibles were the most suitable synthetic approach. Attempts to prepare polycrystalline samples in welded Nb tubes often lead contamination, due to the challenge of having As reacting with the Nb tube[32]. Similar "on-stoichiometry" experiments in open crucibles are hindered by evaporative loses and the formation of other ternary and binary phases[33]. Hence, polycrystalline samples are never pure-phase material. However, this drawback may be circumvented by starting with a suitable precursor or via a prolonged heat-treatment at lower temperature.

These difficulties in synthesizing the title phases are specifically discussed here because there is still room for improvement—notice that while the reactive flux method is overall successful, crystals from multiple phases are often present. In some cases, the products can be distinguished by the morphology (the needle-like $BaIn_2As_2$ crystal can be separated from the blocks of $Ba_3In_2As_4$ [34], a phase which forms at the same conditions and irrespective of the Ba:As nominal ratio). Thus, a few sizable $BaIn_2As_2$ needle-like single crystals of millimeters sizes were extracted and used for some of the physical properties measurements. In the Ca–In–As and Sr–In–As syntheses, using In flux and condition similar to that of $BaIn_2As_2$, crystals of $CaIn_2As_2$ and $SrIn_2As_2$ were synthesized. We note that the phase $SrIn_2As_2$ was reported earlier, apparently from in an attempt to synthesize the $Sr_2In_5As_5$ phase[33]. The crystals could not be distinguished visually and the structural analysis required the screening of a large number of randomly picked specimens. We must also note that small changes in the reaction conditions also contribute to the growth of known "3-2-4" and "3-1-3" phases,[34-36] along with the desired $CaIn_2As_2$ and $SrIn_2As_2$, further complicating the quest to optimize growth parameters and obtain crystals with size suitable for properties measurements.

Crystal structure

The Zintl "1-2-2" compounds ("1-2-2" denotes the compositions AB_2X_2 (A = divalent rare earth or alkaline earth element; B = main group element or d-block metal; X = group 14 or 15 element) crystallize in several main structure types, which largely depend on the choice of B and X atoms. The $BaIn_2P_2$ (space group $P2_1/m$)[18], $BaGa_2Sb_2$ (space group $Pnma$)[37] and $CaBe_2Ge_2$ (space group $P4/nmm$)[38] type structures are seldom observed AB_2X_2 phases. The trigonal $CaAl_2Si_2$ (space group, $P\bar{3}m1$)[39] and the tetragonal $ThCr_2Si_2$ (space group, $I4/mmm$)[40] structure types are most ubiquitous, and have been widely studied. These two structure types have some striking similarities in that both structures are composed of A and B_2X_2 alternate layers with the B atoms forming tetrahedral coordination with the X atoms. However, the BX_4 packing is different for both structure types, with $CaAl_2Si_2$ and $ThCr_2Si_2$ sharing three and four edges with others, respectively.

The "1-2-2" compounds discussed in this paper do not belong to any of the above and form with relatively uncommon structure types. The structures warrant some in depth discussion and will be considered separately in the following paragraphs.

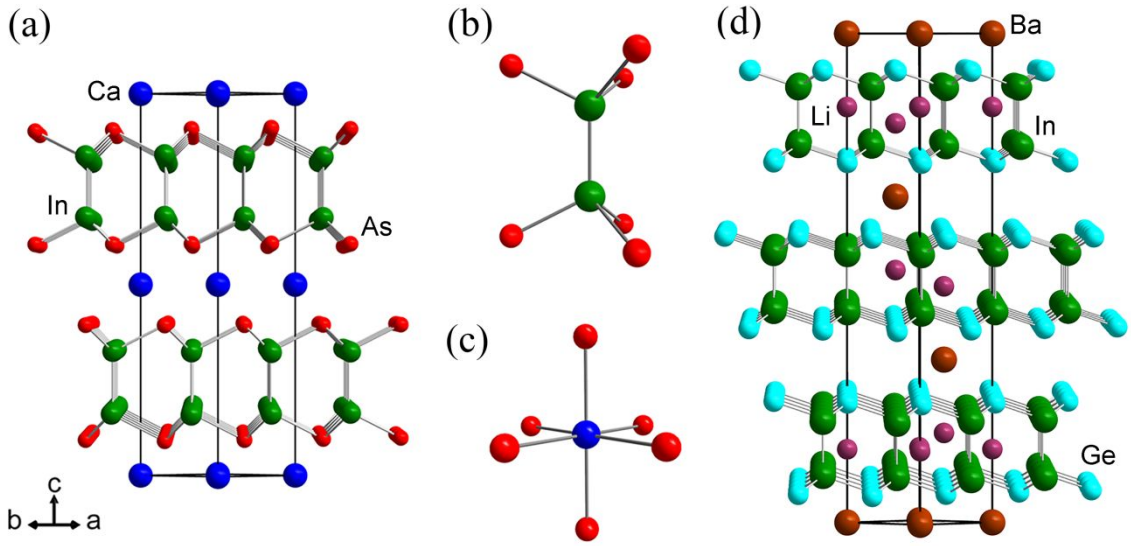

Figure 1. (a): Crystal structure of $CaIn_2As_2$; the layered arrangements of the atoms is emphasized and only In–As bonds are drawn, for clarity. (b): Magnified view of the ethane-like $[In_2As_6]$. (c): Coordination environment of the Ca^{2+} cation. (d): Crystal structure of $BaLi_2In_2Ge_2$, a "1-2-2-2" layered structure exhibiting resemblance of the structural motifs with that of $CaIn_2As_2$.

Table 1. Selected crystallographic data of $CaIn_2As_2$, $SrIn_2As_2$, and $BaIn_2As_2$.

chemical formula	$CaIn_2As_2$	$SrIn_2As_2$	$BaIn_2As_2$
formula weight	419.56	467.10	516.82
temperature		200(2)	
radiation		Mo K_α, 0.71073 Å	
space group	$P6_3/mmc$ (no. 194)	$P6_3/mmc$ (no. 194)	$P2/m$ (no. 10)
a/ Å	4.1482(6)	4.2222(6)	10.2746(11)
b/ Å	4.1482	4.2222	4.3005(5)
c/ Å	17.726(4)	18.110(3)	13.3317(14)
β/°	90	90	95.569(2)
V/ Å^3	264.16(9)	279.59(9)	586.29(11)
Z	2	2	4
ρ_{cal}/ g cm^{-3}	5.28	5.55	5.86
μ/ cm^{-1}	219.5	292.6	254.8
R_1 (I>2σ_I)[a]	0.0132	0.0244	0.0286
wR_2 (I>2σ_I)[a]	0.0280	0.0607	0.0561
R_1 (all data)[a]	0.0211	0.0284	0.0361
wR_2 (all data)[a]	0.0299	0.0618	0.0594
Largest diff. peak and hole	0.57; –0.45	0.76; –1.37	1.98; –1.85

[a] $R_1 = \sum||F_o|-|F_c||/\sum|F_o|$; $wR_2 = [\sum[w(F_o^2 - F_c^2)^2]/\sum[wF_o^2)^2]]^{1/2}$, where $w = 1/[\sigma^2 F_o^2 + (AP)^2 + (BP)]$ and $P = (F_o^2 + 2F_c^2)/3$; A, B are the respective weight coefficients.

Dalton Transactions

ARTICLE

$CaIn_2As_2$ and $SrIn_2As_2$ are isostructural and crystallize in the hexagonal $EuIn_2P_2$ structure type in the $P6_3/mmc$ space group (Z = 2)[16]. Figure 1 presents the schematic view of the crystal structure of $CaIn_2As_2$. The structure consists of three unique crystallographic sites; Ca atoms occupy the 2*a* site with a 3*m* symmetry, while In and As atoms occupy unique 4*f* sites with 3*m* symmetries as shown in Table 2. Like the $CaAl_2Si_2$ structure types, the $EuIn_2P_2$ arrangement is also a layered structure. From the crystal structure of $CaIn_2As_2$ in Figure 1(a), layers of Ca^{2+} cations and $[In_2As_2]^{2-}$ polyanions alternate and are stacked along the *c*-direction. Each In atom is bonded to three As atoms in a pyramidal geometry. Two such moieties are dimerized into ethane-like $As_3In–InAs_3$ units having the eclipsed conformation, as shown in Figure 1(b). As–In–As and As–In–In bond angles in $CaIn_2As_2$ are approx. 101° and 117°, respectively, indicating a significant distortion from the ideal tetrahedral, sp^3-like coordination. For $SrIn_2As_2$ the values for As–In–As and As–In–In bond angles are ca. 102° and 116°, respectively. Similar bond angles are reported in $EuIn_2As_2$[15] (102.6° and 115.7°) and $EuIn_2P_2$[16] (102.6° and 115.7°).

Selected bond lengths are tabulated in Table 3. One will notice that the In–In distances in $CaIn_2As_2$ and $SrIn_2As_2$ are nearly identical, 2.766(1) Å and 2.767(1) Å, respectively. The distances are comparable to the value of 2.85 Å obtained by considering the covalent radius of In (1.425 Å)[41] as well as the reported values of 2.765 Å and 2.762 Å for $EuIn_2As_2$[15] and $SrIn_2P_2$[18], respectively. The values are in excellent agreement with the In–In distances seen in a variety of compounds with In–In bonding that have been reported in the literature. Specifically, 2.762 Å, 2.763 Å, 2.765 Å, and 2.746 Å and 2.816 Å for $SrIn_2P_2$[18], $CaIn_2P_2$[18], $EuIn_2As_2$[15], and $BaIn_2P_2$[18], respectively. The In–As distances of 2.684 Å for $CaIn_2As_2$ and 2.703 Å for $SrIn_2As_2$ are reconcilable to the value of 2.619 Å obtained by summing of the covalent radii of In (1.425 Å) and As (1.194 Å)[41]. The observed distance in $EuIn_2As_2$[15] is 2.695 Å, while in Eu_3InAs_3, the observed distances are in the range of 2.682 Å to 2.704 Å. Other relevant comparisons can be made as well: 2.686 Å to 2.710 Å for Sr_3InAs_3[34], 2.666 Å to 2.772 Å for Ba_3InAs_3[42], and 2.646 Å to 2.741 Å for $Sr_3In_2As_4$[34]. The quoted numbers are indicative of a covalent nature of both In–In and In–As bonds.

The coordination of the Ca/Sr^{2+} cation is by six As^{3-} ions (Ca/Sr–In distances exceed 3.85 Å); the $Ca/SrAs_6$ units are edge-shared in the *ab*-plane (see Figure 1(c) and Figure S1). The Ca/Sr–As distances within the octahedra are 3.018 Å and 3.138 Å long (Table 3). The angles within the octahedra deviate from 90°; they are 86.82° and 93.18° for the $CaIn_2As_2$ structure and 84.55° and 95.45° for $SrIn_2As_2$. This is indicative of a slight distortion from the ideal octahedral geometry (but fully consistent with the hexagonal symmetry).

For further insight into this crystal structure, we can compare the "1-2-2" structure under consideration to that of the "1-2-2-2" layered structure of the quaternary $BaLi_2In_2Ge_2$ phase[43]. The rhombohedral structure of the latter (space group $R\bar{3}m$ (No. 166) with unit cell parameters a = 4.5747(6) Å, c = 26.381(4) Å) is depicted in Figure 1(d) and from the given projections, one can immediately recognize the close structural relationship between the two phases. There are identical 6-membered rings formed by In and As (or Ge) atoms. The relationship between the two structures can also be conceptualized as follows: being a germanide, the polyanions in $BaLi_2In_2Ge_2$ will be assigned as $[In_2Ge_2]^{4-}$, i.e., requiring two additional electrons compared to $[In_2As_2]^{2-}$ with the same topology. These two electrons are contributed by the small Li atoms, which are able to fit within the layers. It should also be noted that similar structural motifs are observed in the structure of the binary GaS compound, which can be considered as the "cation-free" version of the same structure—since these relationships have already been described, for additional information the reader is referred to the discussion in our earlier report[43].

Table 2. Atomic coordinates and equivalent isotropic displacement parameters (U_{eq}[a]) of $CaIn_2As_2$, $SrIn_2As_2$, and $BaIn_2As_2$.

atom	Wyckoff site	*x*	*y*	*z*	U_{eq}/Å^2
		$CaIn_2As_2$			
Ca	2*a*	0	0	0	0.0108(3)
In	4*f*	1/3	2/3	0.17198(2)	0.0103(1)
As	4*f*	1/3	2/3	0.60362(3)	0.0092(1)
		$SrIn_2As_2$			
Sr	2*a*	0	0	0	0.0105(3)
In	4*f*	1/3	2/3	0.17360(3)	0.0109(2)
As	4*f*	1/3	2/3	0.60915(4)	0.0093(3)
		$BaIn_2As_2$			
Ba1	2*n*	0.18569(6)	1/2	0.78568(5)	0.0145(1)
Ba2	1*d*	1/2	0	0	0.0111(1)
Ba3	1*c*	0	0	1/2	0.0110(1)
In1	2*n*	0.20223(7)	1/2	0.33263(5)	0.0121(1)
In2	2*n*	0.41230(7)	1/2	0.22312(5)	0.0121(1)
In3	2*m*	0.11549(7)	0	0.06875(5)	0.0113(1)
In4	2*m*	0.39372(7)	0	0.55810(5)	0.0117(1)
As1	2*n*	0.2336(1)	1/2	0.53432(7)	0.0107(2)
As2	2*n*	0.2697(1)	1/2	0.03730(7)	0.0107(2)
As3	2*m*	0.05609(9)	0	0.26356(7)	0.0110(2)
As4	2*m*	0.57209(9)	0	0.23923(7)	0.0105(2)

[a] U_{eq} is defined as 1/3 of the trace of the orthogonalized U_{ij} tensor

Table 3. Selected interatomic distances in $CaIn_2As_2$, $SrIn_2As_2$ and $BaIn_2As_2$.

$CaIn_2As_2$		$SrIn_2As_2$	
atoms	distances (Å)	atoms	distances (Å)
In—In	2.766(1)	In—In	2.767(1)
In—As (×3)	2.6841(5)	In—As (×3)	2.7027(5)
In—Ca (×3)	3.8769(5)	In—Sr (×3)	3.9782(6)
Ca—As (×6)	3.0182(5)	Sr—As (×6)	3.1384(6)
$BaIn_2As_2$			
atoms	distances (Å)	atoms	distances (Å)
Ba1—Ba1 (×2)	4.3005(5)	Ba2—In2 (×4)	3.8476(6)
Ba1—As1	3.434(1)	Ba3—As1 (×4)	3.2222(8)
Ba1—As2	3.382(1)	Ba3—As3 (×2)	3.259(1)
Ba1—As3 (×2)	3.3029(9)	Ba3—In1 (×4)	3.8496(6)
Ba1—As4 (×2)	3.3304(9)	Ba3—In4 (×2)	4.0443(8)
Ba2—Ba2 (×2)	4.3005(5)	In3—In3	2.854(1)
Ba2—As2 (×4)	3.2707(8)	In3—As2 (×2)	2.7275(8)
Ba2—As4 (×2)	3.203(1)	In3—As3	2.725(1)
In4—As1 (×2)	2.7070(8)	In4—In4	2.797(1)
In4—As4	2.691(1)	In1—In2	2.721(1)
In2—As4 (×2)	2.7008(7)	In1—As1	2.677(1)
In2—As2	2.753(1)	In1—As3 (×2)	2.7309(8)

$BaIn_2As_2$ crystallizes in the monoclinic space group *P*2/*m* (*Z* = 4) and it is isostructural to $EuGa_2P_2$[14]. The crystal structure of $BaIn_2As_2$ is more complex, and is presented schematically in Figure 2. The asymmetric unit is composed of 11 atoms with three Ba atoms, four In atoms, and four As atoms that make up the asymmetric unit as shown in Table 2. The Ba atoms are located at sites 1*c*, 1*d,* and 2*n* with symmetries 2/*m*, 2/*m*, and *m*, respectively. The four In atoms are located at four unique sites, 2*m* (×2) and 2*n* (×2) all with *m* symmetries. Similar to the In sites and symmetries, the four As atoms follow the same pattern. These atoms are also located at four different sites: 2*m* (×2) and 2*n* (×2).

Each In atom is 4-coordinated, as expected. Each has three As and one In atom as closest neighbors. Staggered, ethane-like unit similar to those in $CaIn_2As_2$ and $SrIn_2As_2$ are also observed. Due to the lower symmetry, the distortion from ideal tetrahedral geometry is more pronounced. Two of the In–As bonds are of the same length, while a different As atom is at a different distance (Table 3); the adjoining In atom is the 4th apex at yet another distance.

There are three different ethane-like units making up the $[In_2As_2]^{2-}$ slabs (detailed drawings in Figure S2). The first contains the In1–In2 bond (*d* = 2.721 Å). Attached to the In2 atom, at distances of 2.753 Å and 2.701 Å (×2), are As2 and two As4 atoms, respectively (Table 3). Attached to the In1 atom, at distances of 2.677 Å and 2.731 Å (×2) are As1 and two As3 atoms, respectively. The other two unique ethane-like moieties are simpler to visualize. The In4–In4 bond is 2.797 Å long; the As1 (*d* = 2.707 Å (×2)) and As4 (*d* = 2.691 Å) complete the coordination polyhedron. In a perpendicular direction, In3–In3 are dimerized with the longest bond that measures 2.854 Å. The somewhat wide range of bond lengths for the In–In interactions (2.72 to 2.85 Å) is suggestive of varied strengths of the bonds. Yet, based on the single-bonded radius of In (1.425 Å)[41] and based on the previously mentioned values for other similar compounds with In–In bonding, it is apparent that all three In–In bonds have a typical covalent character.

As a part of the structural discussion, it should also be noted that the ethane-like In_2As_6 units observed in $BaIn_2As_2$ are different from those in $CaIn_2As_2$ and $SrIn_2As_2$ (*vide supra*). They are similar to the staggered In_2P_6 units in $BaIn_2P_2$[18]. Despite that, $BaIn_2P_2$ and $BaIn_2As_2$ are *not* isotypic, as the crystal structure of the latter shows a slight geometric distortion relative to the former. Consequently, even though the periodicity constants of the respective unit cells are alike, $BaIn_2P_2$ crystallizes in the space group $P2_1/m$ with two crystallographically unique Ba atoms, as opposed to the space group *P*2/*m* for $BaIn_2As_2$ in which the structure has three unique crystallographic sites for the Ba atoms (Figure S3).

The $BaIn_2As_2$ structure also exemplifies polyanionic $[In_2As_2]^{2-}$ layers separated by Ba^{2+} cations. The latter (all three independent sites) are coordinated in an octahedral fashion by surrounding As^{3-} anions. As one can notice from Figure 2, the coordination polyhedron for Ba1 is a severely distorted octahedron. The respective Ba1–As distances do not vary widely, and they measure 3.303 Å (×2), 3.330 Å (×2), 3.382 Å, and 3.434 Å. This means that the observed distortion is a manifestation of the low symmetry and a result of the "twist" the In_2As_6 unit makes around Ba1. For comparison, Ba2 and Ba3 octahedra are also slightly distorted, but the Ba2–As and Ba3–As distances are shorter and show lesser dispersion. For Ba2 and Ba3, the distances to closest As are 3.259 Å (×2) (Ba3–As3) and 3.271 Å (×4) (Ba2–As2) and 3.203 Å (×2) (Ba2–As4) and 3.223 Å (×4) (Ba3–As1), respectively.

Irrespective of the subtle differences between the structures of the three "1-2-2" compounds, the valence electrons serving the two arrangements can be partitioned in a similar manner. Considering the homoatomic In–In interaction as a covalent bond, reducing the charge on the In atoms from 3+ to 2+, the following charge-breakdown can be achieved: $[A^{2+}][In^{2+}]_2[As^{3-}]_2$, i.e., a salt-like, valence precise composition is realized. Analogously, the structures can also be rationalized using the Zintl-Klemm formalism[44] as $[(A^{2+})[(4b\text{-}In^{1-})_2(3b\text{-}As^0)_2]$, where the notations 3*b*- and 4*b*- indicate atoms with 3, and 4 covalent bonds, respectively.

The last part of the structural discussion is focused on some parallels that can be drawn between the "1-2-2" structures of the herein presented ternary compounds and some well-known binaries. The analogy between the hexagonal (or trigonal) "1-2-2" structure of $CaIn_2As_2$ and the layered structure of GaS was already mentioned. Obviously, the aliovalent group 15 to group 16 substitution allows for the $[Ga_2S_2]$ layers to be freestanding and simply spaced by a van der Waals gap (due to the homoatomic Ga–Ga bonds, GaS can be considered as $[Ga^{2+}]_2[S^{2-}]_2$). If one were to aliovalently replace S with As, then, to maintain the same type of bonding between Ga and As, the interlayer space must be used to intercalate metals that can donate electrons. The least electronegative alkali or alkaline-earth metals are the ideal candidates. Correspondingly, two alkali metal cations between the layers must be fit (likely impossible from close-packing considerations), or better, a single alkaline-earth metal cation

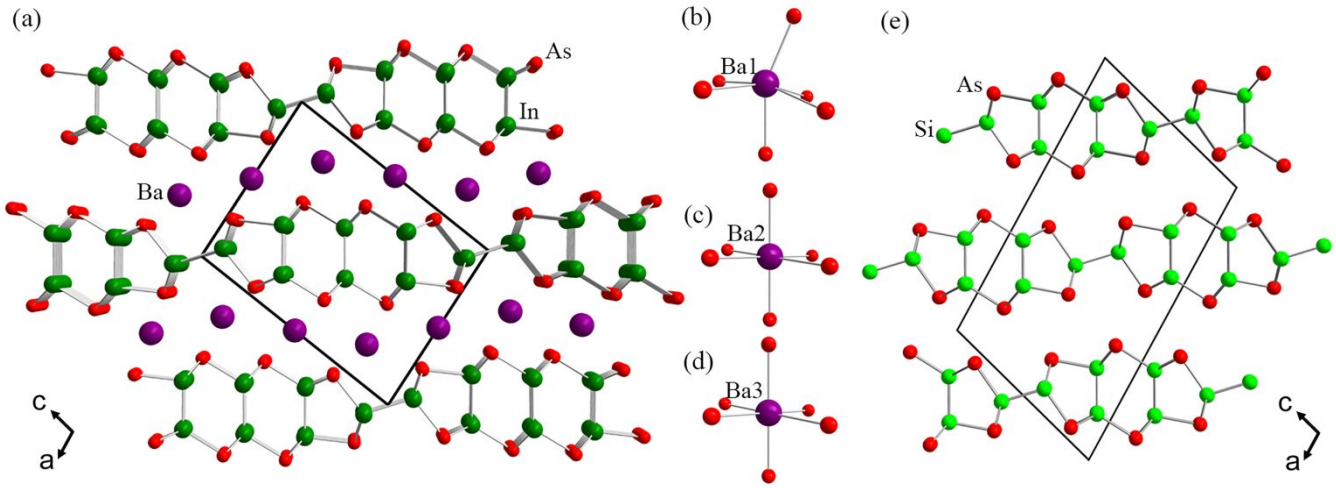

Figure 2. (a) Crystal structure of $BaIn_2As_2$ structure. The layered arrangements of the atoms is emphasized and only In–As bonds are drawn, for clarity. Ba, In, and As atoms occupy multiple independent sites. (b), (c), and (d) Magnified views of coordination environments of the three distinct Ba^{2+} cations. (e) Crystal structure of SiAs, showing the 6- and 5-membered rings formed by Si and As atoms; the similarities between the $BaIn_2As_2$ and SiAs structures are clearly seen.

such as Ca. In the later case, the chemical formula will be $CaGa_2As_2 = [Ca^{2+}][Ga^{2+}]_2[As^{3-}]_2$.

The $BaIn_2As_2$ structure, similarly, can be related to SiAs. The SiAs structure[45], as shown in Figure 2(e) is also monoclinic and it displays the same five-six-five membered rings formed by Si and As atoms, which are linked by Si–Si bonds into layers. Thus, the partitioning of the valence electrons in SiAs follows the scheme $[(Si^{3+})_2(As^{3-})_2]$. The replacement of Si with an electron-poorer In will require the introduction of either alkali metals or alkaline-earth metals. The interlayer spacing can be opened to accommodate such cations and the resultant compounds can be conceptualized by the chemical formula $BaIn_2As_2 = [Ba^{2+}][In^{2+}]_2[As^{3-}]_2$.

Which ternary structure forms—the derivative of GaS or SiAs—must be a function of crystal packing, not electronic factors. For instance, as evidenced by the available experimental data concerning the "1-2-2" compounds with alkaline-earth metals (or the nominally divalent Eu), the hexagonal "1-2-2" structure is preferably formed with smaller to medium sized cations (Ca, Sr, Eu) while the more complex monoclinic structure is an exclusive domain for the large Ba cations.

Electronic structure and chemical bonding

For the purpose of gaining a deeper understanding into the electronic band topology of these compounds, we have carried out electronic structure calculations. Figure 3(a) presents the bulk band structure of $CaIn_2As_2$. The valence band and the conduction band does not cross each other but appears the valence band maximum (VBMa) and the conduction band minimum (CBMi) touch each other along the Γ points to produce a form of band inversion as reported in $EuIn_2As_2$[46]. However, a closer look at the band structure as presented in Figure 3(b) reveals a gapped band structure with a small bandgap E_g = 0.03 eV which is comparable to that of the topological insulator Bi_2Se_3[47]. The observation of a narrow bandgap here likely points at the presence of a nontrivial topological state in $CaIn_2As_2$. While this Zintl phase is nonmagnetic as opposed to $EuIn_2As_2$, which is believed to host an axion insulator, their identical crystal structure appears to provide a robust environment that favors such an exotic state[20,21]. It is expected that such a narrow bandgap could further be tuned in the presence of an applied strain or SOC. Also, the observation of a narrow bandgap here is in favor of the TE properties of this Zintl phase.

Figure 3(c) to (f) show the total and partial density of states (DOS) of $CaIn_2As_2$ with a small bandgap in agreement with the observation in the band structure. The general feature of the band structure and DOS suggests a possibly heavily doped semiconducting character. While the opening of a narrow bandgap is in line with expectations for a closed shell configuration, here it further helps to characterize the topology of the compound. For states near the VBMa, the As-*p* orbital dominates the contributions. The In-*p* character is also significant in this region and suggests a form of covalent nature of As–In interactions. Within the conduction band and near CBMi, it can be observed that both the Ca-*d*, In-*s* and As-*p* provide nearly equal contributions to the electronic states. This observation likely indicates the important role of the three orbital states in both the transport properties. Additional intuitions into the nature of orbital mixing and bonding in this compound can be gained by considering Figure 3(d) to (f). Within the valence band and for energies in the proximity of the Fermi level (−4.0 to 0 eV), As-*p* and In-*p* dominate the electronic character with Ca having only a little contribution. Further down in energy (−6.8 to −4.6 eV), In-*s* contribution is

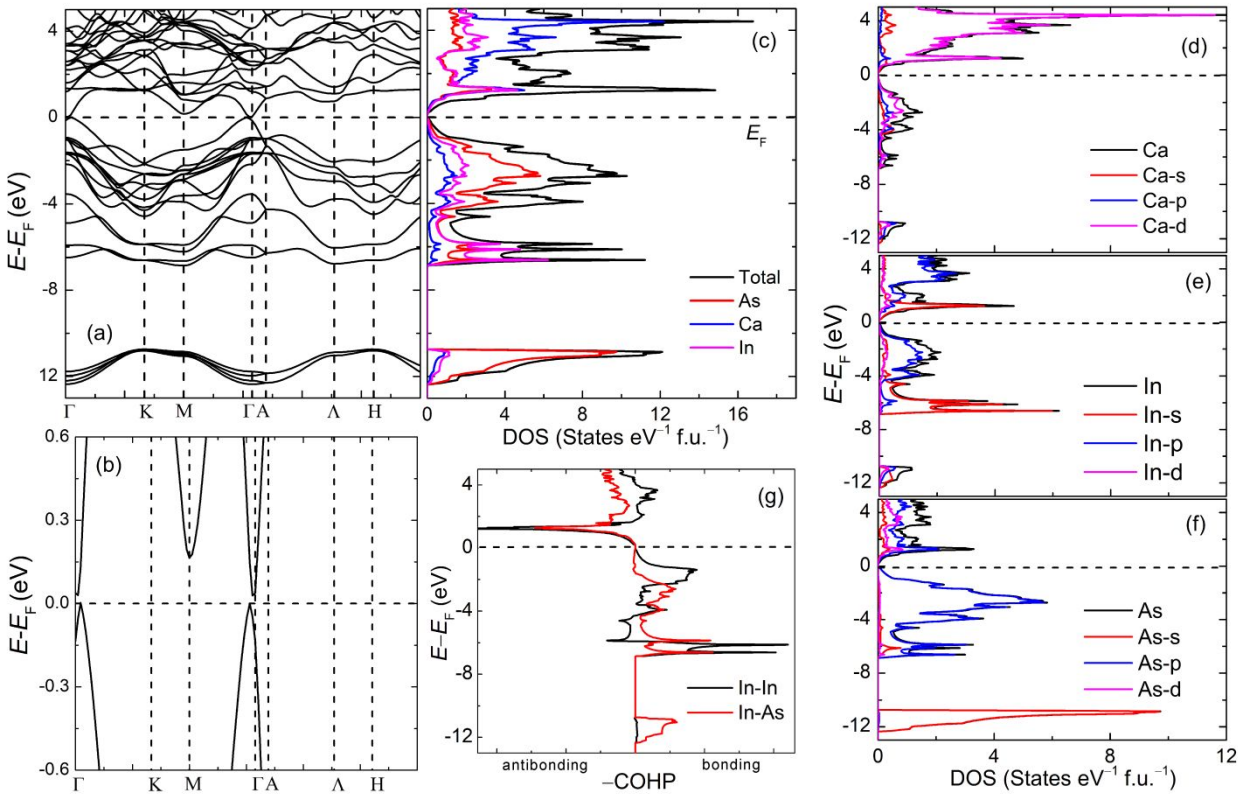

Figure 3. (a): Calculated bulk electronic band structure of $CaIn_2As_2$ along high symmetry directions. The Fermi level is taken as $E-E_F = 0$ and represented with dashed lines. (b): A zoomed-in view of the band structure for small energy window close to the Fermi level which reveals a small direct band gap opening along the Γ point. (c): Total density of states of $CaIn_2As_2$ together with the partial density of states for Ca, In and As. (d) to (f) Orbital resolved partial DOS curves. (g): COHP curves evaluated for the average In—In and As—As bonds.

most significant, followed by that of As-*p* while the contribution from Ca is far lesser compared to the other two. This observation provides a notion of strong admixing between As and In.

A better insight into the bonding character of As—In interaction is provided in Figure 3(g) by the COHP plots. No bonding or antibonding levels cross the Fermi level which is an indication of an optimized electronic structure. Both In—In and As—In interactions show antibonding character with the former having the strongest character as seen at 1.2 eV in the conduction band. Bonding character of the In—In interactions still exists in the energy range from 1 to 2 eV. This notion is buttressed by the character of In—In interaction in the valence band where a strong bonding character is evidenced at −1.4 eV and −6.2 to −6.6 eV. The integrated COHP, −ICOHP for In–In and In–As bonds are 1.881 and 1.930, respectively, which correlate with the notion of their covalent bonding. The As—Ca −ICOHP value of 0.760 on the other hand indicates significant electron transfer and larger degree of ionicity, as expected.

The electronic structure of $SrIn_2As_2$ is very similar to that of $CaIn_2As_2$ and the results from the calculations are presented in Figure S4 in supporting information. The DOS is qualitatively identical to that of $CaIn_2As_2$ in many ways and as such the two compounds are expected to exhibit similar properties. A gapped structure at the Γ-points also of magnitude of ca. 0.03 eV is observed. Similar to the case in $CaIn_2As_2$, the notion of a strong In—As covalent bonding is reinforced. For valence band states in the neighborhood of the Fermi level, As-*p* orbital dominates the other contributions. The next significant contribution is from In-*p* character with the least contribution coming from Sr-*d* orbital. Also, for orbitals close to CBMi, the In-*s*, As-*p* and Sr-*d* characters are observed in the order of their contributions, respectively. This observation likely indicates the important role of the three orbital states in both the transport and magnetic properties as earlier observed for $CaIn_2As_2$. The −ICOHP for In—In, In—As, and As—Sr bonds are 1.951, 1.941, and 0.713, respectively. Here also, the −ICOHP values are in support of covalent bonding characters in the former two and a level of ionicity in the latter.

We present the results from the electronic structure calculation of monoclinic $BaIn_2As_2$ in Figure 4. The band structure of $BaIn_2As_2$ shown in Figure 4(a) is different from those of previously discussed $CaIn_2As_2$ and $SrIn_2As_2$, which is not surprising since $BaIn_2As_2$ crystallizes with a different structure type (*vide supra*). A direct energy bandgap of 0.21 eV (see Figure 4(b) is observed at the D-point, which is about an order of magnitude higher than those of the other two compounds. This value is however reconcilable with those of other arsenides in the range of 0.2 to 0.5 eV [33,34,48]. Interestingly, this value is comparable to that of another TI

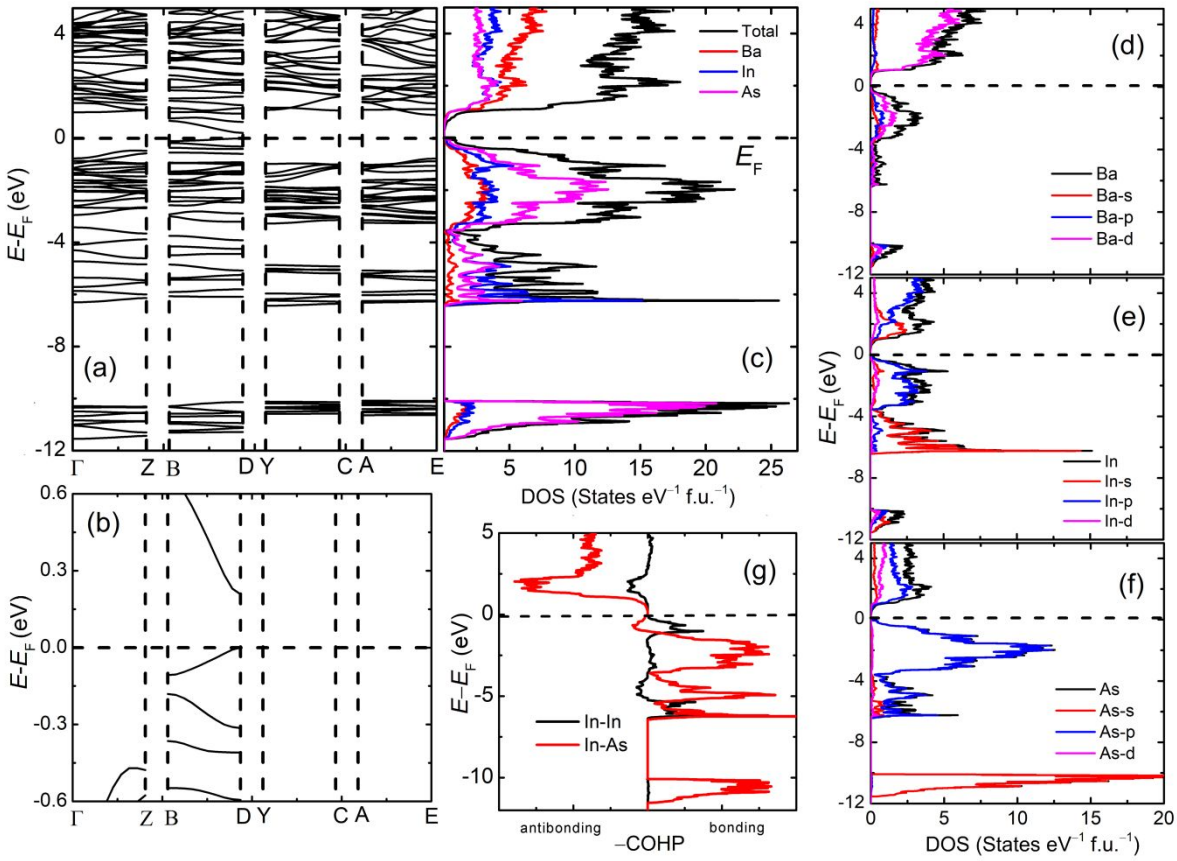

Figure 4. (a): Calculated bulk electronic band structure of $BaIn_2As_2$ along high symmetry directions. The Fermi level is taken as $E-E_F = 0$ and represented with dashed lines. (b): A zoomed-in view of the band structure for small energy window close to the Fermi level which reveals a small direct band gap opening along the Γ point. (c): Total density of states of $BaIn_2As_2$ together with the partial density of states for Ba, In and As. (d) to (f) Orbital resolved partial DOS curves. (g): COHP curves evaluated for the average In–In and As–As bonds.

candidate $Ba_{11}Cd_8Bi_{14}$[47,49]. We note that the magnitude of the bandgap in $BaIn_2As_2$ together with the behavior observed in the electrical resistivity (*vide infra*) are conducive for the realization of excellent TE properties as well as hosting a nontrivial topological state[5,8].

The total and partial DOS curves are shown in Figure 4(c). The As-*p* orbital dominate the contributions near the VBMa while contributions from In-*p* and Ba-*d* orbitals are comparable in this region. However, the Ba-*d* orbitals appear to contribute the most to the DOS in the conduction band. In Figure 4(d) to (f), the orbital resolved partial density of states is presented. The DOS in the energy range of −3.5 to 0 eV is dominated by As-*p* orbitals. Also, within this same energy window, the In-*p* orbital is also significant with the Ba-*d* orbital showing the least contribution. In the energy window of −6.4 to −3.5 eV, the In-*s* orbital shows a significant peak in comparison to contributions from those of As and Ba. The observation here is again signifying a covalent nature of the In–As bonds in $BaIn_2As_2$.

Figure 4(g) presents the COHP plots for the In–In and In–As interactions. Here, the In–As interactions do not appear to be fully optimized as they retain some antibonding character near the Fermi level (window of −1 to 0 eV). In–As bonding in the energy range of 1.35 to 2.6 eV shows a strong antibonding character. In–In interaction also reveals some form of antibonding character in this energy range, albeit very small in comparison to that of In–As. Within the bonding levels (−1.2 to −6.0 eV), several peaks indicating the In–As bond can be observed which outweighs the antibonding character. The bonding character of In-In interaction is also observed and important in this compound. The −ICOHP value for In–In and In–As bonds are 1.960 and 1.930, which are comparable to those of $CaIn_2As_2$ and $SrIn_2As_2$ phases.

Transport properties

Considering the calculated narrow band gaps in the three phases, and which are comparable to those observed for some excellent TE Zintl phases, it is expected that these compounds will show promising transport properties. Because the crystals of $CaIn_2As_2$ and $SrIn_2As_2$ were tiny, and as such, not suitable for measurements, the transport properties could not be determined. The crystals from $BaIn_2As_2$ were also small in general, but we managed to isolate few ones that are of dimensions allowing for transport properties measurements; the data are presented below.

Electrical resistivity

The temperature dependence of the electrical resistivity $\rho(T)$ of $BaIn_2As_2$ is shown in Figure 5(a). The data presented shows both the cooling and heating cycles in the temperature range of 10 to 300 K. The numerical values are nearly identical thus, revealing the complete reversibility of $\rho(T)$. The observed residual resistivity ratio ρ_{300}/ρ_{10} is approx. 3, which is indicative of the quality of our sample. At room temperature, ρ-value is 0.75 mΩ·cm, which is comparable to those observed in similar semiconducting materials. This observation is in agreement with the bandgap opening in $BaIn_2As_2$ seen from the electronic structure calculations, as well as with the discussed closed-shell electronic configurations for all atoms, based on the Zintl-Klemm formalism.

However, upon cooling from room temperature, $\rho(T)$ decreases with temperature—a behavior reminiscent of the simple metals. This anomalous $\rho(T)$ dependence classifies $BaIn_2As_2$ as a heavily doped semiconductor—an effect that has found several applications[50,51]. Here, $BaIn_2As_2$ is a p-type semiconductor (vide infra) and as such, it is expected that an acceptor impurity would contribute hole levels slightly above the Fermi level (within the band gap) thereby making it easy for electrons to move into these levels from the valence band. Consequently, the position of the Fermi level (effective) is re-adjusted to be at an intermediate position between the valence band and the acceptor levels. The E_g = 0.28 eV in $BaIn_2P_2$[52] is comparable to that of $BaIn_2As_2$, although it is not clear whether this phase is also a degenerate semiconductor since no experimental transport properties have been reported.

Furthermore, the exhibition of a heavily doped (degenerate) semiconducting behavior is reminiscent of several high-performance thermoelectric (TE) materials[8] and as such further reaffirm the promising of the $BaIn_2As_2$ phase for thermoelectrics development. At low temperatures, below ~16 K, $\rho(T) \sim AT^2$ where A is the coefficient of the quadratic term in resistivity and suggests the realization of a possible Fermi liquid behavior.

Thermopower

To probe the thermoelectric (TE) properties of $BaIn_2As_2$, the Seebeck coefficient, α, was measured on a small needle-like crystal. Figure 5(b) presents the temperature dependence of the Seebeck coefficient for temperatures between 300 and 600 K. $\alpha(T)$ has positive slope in the studied temperature range, indicating a p-type semiconductor where the holes are the dominant charge carriers. The data reveals a relatively low α value of 4.8 μV/K at room temperature; at 600 K a value of 21 μV/K is achieved, which is nearly an order of magnitude lower than values achieved in state of the art TE materials[53]. The gradual rise in $\alpha(T)$ around 450 K likely suggests a reduction in the concentration of the minority charge carriers in this region thus leading to a conspicuous rise in $\alpha(T)$ as observed. This assertion seems reasonable since the holes are expected to be thermally activated at such a high temperature. It is noted that at 600 K, $\alpha(T)$ still shows a strong tendency to increase to higher values at elevated temperatures. At this time, the intrinsic nature of such an anomaly in $\alpha(T)$ cannot be fully ascertained as it could also be an artifact in our measurement—what is clear from this result is the nature of the dominant carriers in this phase. In any case, it is expected that the TE properties of this material will be revisited as at when suitable single crystals can be synthesized which will allow us to further investigate its intrinsic TE properties.

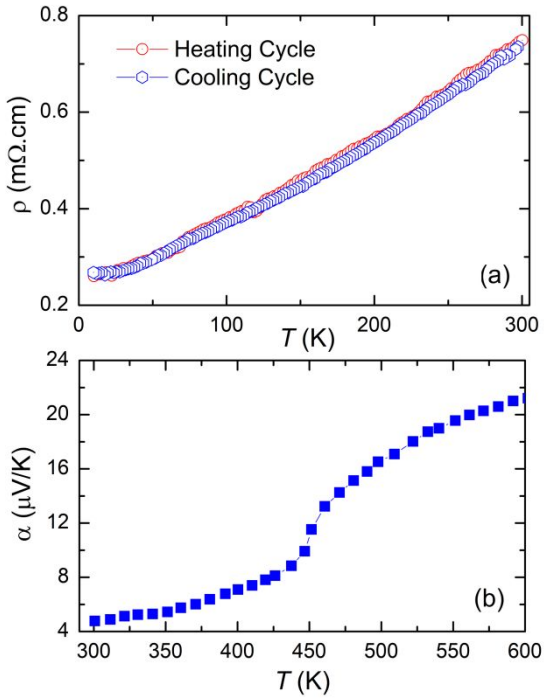

Figure 5. (a): $\rho(T)$ of single-crystalline $BaIn_2As_2$. (b): $\alpha(T)$ of single-crystalline $BaIn_2As_2$.

Experimental

Synthesis

Single crystals of $CaIn_2As_2$, $SrIn_2As_2$ and $BaIn_2As_2$ were synthesized by In-flux reaction. The elements Ca/Sr:In:As and Ba:In:As were weighed in the ratio of 1:25:2 and 3:25:4, respectively, inside an Ar-filled glovebox. All the elements used were purchased from Sigma-Aldrich and Alfa-Aesar with typical purity of ≥99.9 wt.%. The weighed elements were loaded into alumina crucibles which were packed between two balls of quartz wool and encased in a fused silica tube that was subsequently evacuated and flame-sealed under vacuum. The tubes were placed into a muffle furnace in an upright manner, where the elemental mixtures were heated to 1273 K at a rate of 100 K/h and homogenized at this temperature for 20 h. Then, temperature was lowered to 773 K at the rate of 4 K/h. Upon reaching this temperature, the fused-silica tubes were removed from the furnace, flipped, and spun in a centrifuge at high speed to remove excess molten In. The tubes were then taken to the Ar-filled glove box to extract the crystals. Small crystals of $CaIn_2As_2$ and $SrIn_2As_2$ with hexagonal facets, as well

as needle-like $BaIn_2As_2$ crystals were identified. It should be noted that the reaction that produced $BaIn_2As_2$ also yielded $Ba_3In_2As_4$[34]. Similarly, the reactions that produced the $CaIn_2As_2$ and $SrIn_2As_2$ phases allowed the growth of multiple other phases, among them the "3-2-4" phases[34,35], "3-1-3" [36] phases, as well as binary InAs. No conditions (between T_{max} 1233 K and 1373 K) yielding a single-phase product or larger crystals were found. We also observed that reactions using Pb flux reproduced these phases. Several attempts aimed at using Sn flux were made but were not successful.

Powder X-ray diffraction (PXRD)

PXRD measurements were conducted at room temperature on a Rigaku Miniflex diffractometer (filtered Cu K_α radiation, λ = 1.5418 Å), which is operated inside a nitrogen-filled glovebox. Small portions of the obtained single crystals were ground inside an argon-filled glove box using agate mortars and pestles. Data were collected between 5 and 75° in 2θ with a step size of 0.05° and 2 s/step counting time. The powder diffraction patterns were matched with the theoretically generated patterns (based on the crystal structures that were elucidated based on single-crystal X-ray diffraction methods), which confirmed that the bulk of the phase is the target composition.

PXRD measurements before and after exposure to air indicate that $CaIn_2As_2$, $SrIn_2As_2$ and $BaIn_2As_2$ are not stable in air.

Single-crystal X-ray diffraction (SCXRD)

Single-crystal X-ray diffraction experiments were performed on a Bruker APEX-II CCD diffractometer equipped with a Mo K_α radiation (λ = 0.71073 Å) source. Single crystals from the prepared samples were immersed in Paratone-N oil and cut into suitable dimensions. The selected single crystal was placed onto a low-background plastic loop holder, quickly moved to the goniometer maintained at 200 K for the whole period of data collection. Measurements were carried out in batch runs with a frame width of 0.8° in ω and θ with data collections using a Bruker software. SADABS software was used for multi-scan absorption correction. Structure solution and refinements were carried out using ShelXT[54] and ShelXL[55] (integrated into Olex2[56] graphical user interface), respectively. STRUCTURE TIDY[57] software was used to standardize the atomic coordinates. Selected crystallographic data of the three reported phases are tabulated in Tables 1 and 2. Files with deposition numbers CSD 2082408, 2082409, and 2082410 contain the supplementary crystallographic data for this paper. These data can be obtained free of charge via www.ccdc.cam.ac.uk/data_request/cif or by emailing data_request@ccdc.cam.ac.uk, or by contacting The Cambridge Crystallographic Data Centre, 12 Union Road, Cambridge CB2 1EZ, UK; fax: +44 1223 336033.

Electronic structure calculations

Electronic structure calculations were performed on $CaIn_2As_2$, $SrIn_2As_2$ and $BaIn_2As_2$ by utilizing the Tight-Binding Linear Muffin-Tin Orbital (TB-LMTO)-Atomic Sphere Approximation (ASA) code[58] implemented within the Density Functional Theory (DFT) framework. The von Barth-Hedin implementation of the local density approximation (LDA) functional was used while the tetrahedron method[59] was utilized for *k*-space integrations with Brillouin zone samplings of 24×24×8, 18×18×4 and 12×36×12 *k*-point grids for $CaIn_2As_2$, $SrIn_2As_2$ and $BaIn_2As_2$, respectively. For the calculations, an introduction of empty spheres was necessary to satisfy the ASA condition. We have used the determined unit cell parameters and atomic positions for the calculations. The basis set taken for the calculations include the following orbitals: 4*s*, [4*p*], 3*d*, for Ca, 5*s*, 5*p*, [5*d*], [4*f*] for In, 4*s*, 4*p*, [4*d*] for As, [5*p*], 4*d*, [4*f*] for Sr, and 6*s*, [6*p*], 5*d*, 4*f* for Ba. The downfolded orbitals are shown in brackets and are treated with the Löwdin technique. Chemical bonding analyses were carried out based on calculations of the energy contributions of all the filled electronic states for selected pairs of atoms based on the Crystal Orbital Hamilton Population (COHP) method[60] available within the LMTO-ASA code.

Physical property measurements

Electrical transport measurements were carried out on a single crystal of $BaIn_2As_2$ using a conventional four-probe method on a Quantum Design Physical Property Measurement System (Quantum Design Inc., San Diego). Silver wire contacts were made using a high-purity silver conductive paint, obtained from SPI Supplies on appropriate geometry of the sample. Adequate precautions were taken to limit the exposure of the sample to air during the entire process. Data were collected in the temperature range of 10 to 300 K for both cooling and heating cycles. Seebeck coefficient measurement on a single crystal of $BaIn_2As_2$ was measured using the integral method and a constantan wire used as a reference on a SB-100 module MMR Tech. instrument. Appropriate geometry of the sample was mounted on the platform using a high-purity silver conductive paint and interfaced with the probe using the same silver conductive paint. Data were collected for temperatures between 300 to 600 K with the sample exposed to limited amount of air throughout the whole process.

Conclusions

Three new ternary indium arsenides—$CaIn_2As_2$, $SrIn_2As_2$, and $BaIn_2As_2$ have been synthesized and their crystal structures elucidated from single crystal X-ray diffraction. $CaIn_2As_2$ and $SrIn_2As_2$ are isostructural and crystallize in the hexagonal crystal system with the space group $P6_3/mmc$ while $BaIn_2As_2$ crystallizes in the monoclinic crystal system with the space group $P2/m$. Bulk electronic structure calculation on the three compounds show $CaIn_2As_2$ and $SrIn_2As_2$ to have very small E_g of about 0.03 eV along the Γ point, thus making them a rare type of narrow band-gap semiconductors. The electronic structure of the monoclinic $BaIn_2As_2$ indicates a band gap of 0.21 eV along the D-point, which is nearly an order of magnitude higher than the observed value in Ca and Sr-based compounds. Similar to $CaIn_2As_2$ and $SrIn_2As_2$, $BaIn_2As_2$ is also a narrow band-gap semiconductor. The semiconducting signature observed based on the electronic structure calculations in the three compounds is in conformity to the Zintl-Klemm formalism. Preliminary transport properties on $BaIn_2As_2$

indicate it is a degenerate p-type semiconductor and that it holds the potentials of showing properties of interest.

While the electrical and transport properties of $CaIn_2As_2$ and $SrIn_2As_2$ are not immediately available due to the unavailability of suitable crystals for measurements, efforts are being put in place to optimize their syntheses so as to allow for the investigation of their thermoelectric properties. As noted earlier there exists a close relationship between the properties of TIs and TE materials. Hence, these phases will provide an open window to exploring both the topological and TE properties, where the *zT* value can be optimized at an operating temperature by fine-tuning some of the surface properties.

Lastly, there are only a handful of reported ternary phases in the Ba-In-As phase diagram namely; Ba_3InAs_3[42], $Ba_2In_5As_5$[33] and $Ba_3In_2As_4$[34], and as such, our report on $BaIn_2As_2$ phase serves to add to the number of known phases in this phase diagram. In the Ca-In-As phase diagram, only $Ca_3In_2As_4$[35] phase is reported while for Sr-In-As phase diagram, $Sr_5In_2As_6$[34], $Sr_3In_2As_4$[34] and $Sr_{15}In_{22}As_{32}$[61] phases have been reported. In the same vein, our report on $CaIn_2As_2$ and $SrIn_2As_2$ adds to the scanty known phases with the $EuIn_2P_2$ type structure as well as provide us with ample opportunities to investigate their topological and TE properties.

Author contributions

The manuscript was written through contributions of all authors. All authors have given approval to the final version of the manuscript.

Conflicts of interest

There are no conflicts to declare.

Acknowledgements

This work was supported by the U.S. Department of Energy, Office of Science, Basic Energy Sciences through grant DE-SC0008885.

Notes and references

1 M. Z. Hasan and C. L. Kane, *Rev. Mod. Phys.*, 2010, **82**, 3045–3067.
2 K. v. Klitzing, G. Dorda and M. Pepper, *Phys. Rev. Lett.*, 1980, **45**, 494–497.
3 D. J. Thouless, M. Kohmoto, M. P. Nightingale and M. den Nijs, *Phys. Rev. Lett.*, 1982, **49**, 405–408.
4 C. Day, *Phys. Today*, 2008, **61**, 19–23.
5 L. Müchler, H. Zhang, S. Chadov, B. Yan, F. Casper, J. Kübler, S.-C. Zhang and C. Felser, *Angew. Chem. Int. Ed.*, 2012, **51**, 7221–7225.
6 Y. Fan and K. L. Wang, *SPIN*, 2016, **06**, 1640001.
7 M. He, H. Sun and Q. L. He, *Front. Phys.*, 2019, **14**, 43401.
8 L. Müchler, F. Casper, B. Yan, S. Chadov and C. Felser, *Phys. Status Solidi - Rapid Res. Lett.*, 2013, **7**, 91–100.
9 N. Xu, Y. Xu and J. Zhu, *npj Quantum Mater.*, 2017, **2**, 51.
10 K. Pal, S. Anand and U. V. Waghmare, *J. Mater. Chem. C*, 2015, **3**, 12130–12139.
11 Y. Xu, Z. Gan and S.-C. Zhang, *Phys. Rev. Lett.*, 2014, **112**, 226801.
12 S. Roychowdhury, M. Samanta, A. Banik and K. Biswas, *J. Solid State Chem.*, 2019, **275**, 103–123.
13 E. Zintl and W. Dullenkopf, *Z. Phys. Chem.*, 1932, **16B**, 183–194.
14 A. M. Goforth, H. Hope, C. L. Condron, S. M. Kauzlarich, N. Jensen, P. Klavins, S. MaQuilon and Z. Fisk, *Chem. Mater.*, 2009, **21**, 4480–4489.
15 A. M. Goforth, P. Klavins, J. C. Fettinger and S. M. Kauzlarich, *Inorg. Chem.*, 2008, **47**, 11048–11056.
16 J. Jiang and S. M. Kauzlarich, *Chem. Mater.*, 2006, **18**, 435–441.
17 N. Singh and U. Schwingenschlögl, *Appl. Phys. Lett.*, 2012, **100**, 151906.
18 J. F. Rauscher, C. L. Condron, T. Beault, S. M. Kauzlarich, N. Jensen, P. Klavins, S. MaQuilon, Z. Fisk and M. M. Olmstead, *Acta Crystallogr. C*, 2009, **65**, i69–i73.
19 N. Guechi, A. Bouhemadou, A. Guechi, M. Reffas, L. Louail, A. Bourzami, M. Chegaar and S. Bin-Omran, *J. Alloys Compd.*, 2013, **577**, 587–599.
20 Z. Wang, G. Wang, X. Shi, D. Wang and X. Tian, *J. Phys. D. Appl. Phys.*, 2017, **50**, 465304.
21 H. Wang, X. Zhu, Z. Chen, F. Lu, H. Li, Y. Han, L. Li, W. Gao, W. Ning and M. Tian, *J. Phys. Condens. Matter*, DOI:10.1088/1361-648X/abe96d.
22 H. Li, S.-Y. Gao, S.-F. Duan, Y.-F. Xu, K.-J. Zhu, S.-J. Tian, J.-C. Gao, W.-H. Fan, Z.-C. Rao, J.-R. Huang, J.-J. Li, D.-Y. Yan, Z.-T. Liu, W.-L. Liu, Y.-B. Huang, Y.-L. Li, Y. Liu, G.-B. Zhang, P. Zhang, T. Kondo, S. Shin, H.-C. Lei, Y.-G. Shi, W.-T. Zhang, H.-M. Weng, T. Qian and H. Ding, *Phys. Rev. X*, 2019, **9**, 041039.
23 H.-C. Chen, Z.-F. Lou, Y.-X. Zhou, Q. Chen, B.-J. Xu, S.-J. Chen, J.-H. Du, J.-H. Yang, H.-D. Wang and M.-H. Fang, *Chin. Phys. Lett.*, 2020, **37**, 047201.
24 M. Marshall, I. Pletikosić, M. Yahyavi, H.-J. Tien, T.-R. Chang, H. Cao and W. Xie, *J. Appl. Phys.*, 2021, **129**, 035106.
25 S. Pakhira, M. A. Tanatar and D. C. Johnston, *Phys. Rev. B*, 2020, **101**, 214407.
26 F. Kabir, M. M. Hosen, F. C. Kabeer, A. Aperis, X. Ding, G. Dhakal, K. Dimitri, C. Sims, S. Regmi, L. Persaud, K. Gofryk, P. M. Oppeneer, D. Kaczorowski and M. Neupane, *arxiv:1912.08645*.
27 J. Ma, H. Wang, S. Nie, C. Yi, Y. Xu, H. Li, J. Jandke, W. Wulfhekel, Y. Huang, D. West, P. Richard, A. Chikina, V. N. Strocov, J. Mesot, H. Weng, S. Zhang, Y. Shi, T. Qian, M. Shi and H. Ding, *Adv. Mater.*, 2020, **32**, 1907565.
28 J.-Z. Ma, S. M. Nie, C. J. Yi, J. Jandke, T. Shang, M. Y. Yao, M. Naamneh, L. Q. Yan, Y. Sun, A. Chikina, V. N. Strocov, M. Medarde, M. Song, Y.-M. Xiong, G. Xu, W. Wulfhekel, J. Mesot, M. Reticcioli, C. Franchini, C. Mudry, M. Müller, Y. G. Shi, T. Qian, H. Ding and M. Shi, *Sci. Adv.*, 2019, **5**, eaaw4718.
29 N. H. Jo, B. Kuthanazhi, Y. Wu, E. Timmons, T.-H. Kim, L. Zhou, L.-L. Wang, B. G. Ueland, A. Palasyuk, D. H. Ryan, R. J. McQueeney, K. Lee, B. Schrunk, A. A. Burkov, R. Prozorov, S. L. Bud'ko, A. Kaminski and P. C. Canfield, *Phys. Rev. B*, 2020, **101**, 140402.
30 C. Niu, N. Mao, X. Hu, B. Huang and Y. Dai, *Phys. Rev. B*, 2019, **99**, 235119.
31 H. Wang, N. Mao, X. Hu, Y. Dai, B. Huang and C. Niu, *Mater. Horiz.*, 2021, **8**, 956–961.
32 S. Baranets, H. He and S. Bobev, *Acta Crystallogr. Sect. C Struct. Chem.*, 2018, **74**, 623–627.
33 J. Mathieu, R. Achey, J.-H. Park, K. M. Purcell, S. W. Tozer and S. E. Latturner, *Chem. Mater.*, 2008, **20**, 5675–5681.
34 A. B. Childs, S. Baranets and S. Bobev, *J. Solid State Chem.*, 2019, **278**, 120889.
35 G. Cordier, H. Schäfer and M. Stelter, *Z. Naturforsch. B*, 1986, **41**, 1416–1419.
36 K. Rajput, S. Baranets and S. Bobev, *Chem. Mater.*, 2020, **32**, 9616–9626.
37 S.-J. Kim and M. G. Kanatzidis, *Inorg. Chem.*, 2001, **40**, 3781–3785.

38 C. Zheng and R. Hoffmann, *J. Am. Chem. Soc.*, 1986, **108**, 3078–3088.
39 H.-G. von Schnerring, C. Zheng, R. Hoffmann and R. Nesper, *J. Am. Chem. Soc.*, 1986, **108**, 1876–1884.
40 Z. Ban and M. Sikirica, *Acta Crystallogr.*, 1965, **18**, 594–599.
41 B. Cordero, V. Gómez, A. E. Platero-Prats, M. Revés, J. Echeverría, E. Cremades, F. Barragán and S. Alvarez, *Dalt. Trans.*, 2008, 2832–2838.
42 M. Somer, W. Carrillo-Cabrera, K. Peters, H. G. Schnering and G. Cordier, *Z. Krist.*, 1996, **221**, 632–632.
43 A. Ovchinnikov and S. Bobev, *Inorg. Chem.*, 2019, **58**, 7895–7904.
44 R. Nesper, *Z. Anorg. Allg. Chem.*, 2014, **640**, 2639–2648.
45 T. Wadsten, S. Burmester, G. Cederberg, R. B. Jensen, C. T. Pederson and E. Larsen, *Acta Chem. Scand.*, 1965, **19**, 1232–1238.
46 S. Regmi, M. M. Hosen, B. Ghosh, B. Singh, G. Dhakal, C. Sims, B. Wang, F. Kabir, K. Dimitri, Y. Liu, A. Agarwal, H. Lin, D. Kaczorowski, A. Bansil and M. Neupane, *Phys. Rev. B*, 2020, **102**, 165153.
47 F. Tang, H. C. Po, A. Vishwanath and X. Wan, *Nature*, 2019, **566**, 486–489.
48 H. He, R. Stearrett, E. R. Nowak and S. Bobev, *Eur. J. Inorg. Chem.*, 2011, **2011**, 4025–4036.
49 S.-Q. Xia and S. Bobev, *Inorg. Chem.*, 2006, **45**, 7126–7132.
50 R. A. Abram, G. J. Rees and B. L. H. Wilson, *Adv. Phys.*, 1978, **27**, 799–892.
51 V. I. Fistul, *Heavily Doped Semiconductors*, Springer New York, Boston, MA, 1995.
52 N. Guechi, A. Bouhemadou, R. Khenata, S. Bin-Omran, M. Chegaar, Y. Al-Douri and A. Bourzami, *Solid State Sci.*, 2014, **29**, 12–23.
53 S. R. Brown, S. M. Kauzlarich, F. Gascoin and G. J. Snyder, *Chem. Mater.*, 2006, **18**, 1873–1877.
54 G. M. Sheldrick, *Acta Crystallogr. A*, 2015, **71**, 3–8.
55 G. M. Sheldrick, *Acta Crystallogr. C*, 2015, **71**, 3–8.
56 O. V. Dolomanov, L. J. Bourhis, R. J. Gildea, J. A. K. Howard and H. Puschmann, *J. Appl. Crystallogr.*, 2009, **42**, 339–341.
57 L. M. Gelato and E. Parthé, *J. Appl. Crystallogr.*, 1987, **20**, 139–143.
58 O. Jepsen and O. K. Andersen, *The STUTTGART TB-LMTO-ASA program*, Max-Planck-Institut für Festkörperforschung, Stuttgart, Germany, 1999.
59 P. E. Blöchl, O. Jepsen and O. K. Andersen, *Phys. Rev. B*, 1994, **49**, 16223–16233.
60 R. Dronskowski and P. E. Blöchl, *J. Phys. Chem.*, 2002, **97**, 8617–8624.
61 V. Weippert, A. Haffner, A. Stamatopoulos and D. Johrendt, *J. Am. Chem. Soc.*, 2019, **141**, 11245–11252.